PHYSICAL REVIEW E **91**, 062204 (2015)

Network flow model of force transmission in unbonded and bonded granular media

Antoinette Tordesillas and Steven T. Tobin
School of Mathematics and Statistics, The University of Melbourne, Melbourne VIC 3010, Australia

Mehmet Cil and Khalid Alshibli
Department of Civil and Environmental Engineering, University of Tennessee, Knoxville, Tennessee 37996, USA

Robert P. Behringer
Department of Physics, Duke University, Durham, North Carolina 27708, USA

(Received 5 February 2015; published 8 June 2015)

An established aspect of force transmission in quasistatic deformation of granular media is the existence of a dual network of strongly versus weakly loaded particles. Despite significant interest, the regulation of strong and weak forces through the contact network remains poorly understood. We examine this aspect of force transmission using data on microstructural fabric from: (I) three-dimensional discrete element models of grain agglomerates of bonded subspheres constructed from *in situ* synchrotron microtomography images of silica sand grains under unconfined compression and (II) two-dimensional assemblies of unbonded photoelastic circular disks submitted to biaxial compression under constant volume. We model force transmission as a network flow and solve the maximum flow–minimum cost (MFMC) problem, the solution to which yields a percolating subnetwork of contacts that transmits the "maximum flow" (i.e., the highest units of force) at "least cost" (i.e., the dissipated energy from such transmission). We find the MFMC describes a two-tier hierarchical architecture. At the local level, it encapsulates intraconnections between particles in individual force chains and in their conjoined 3-cycles, with the most common configuration having at least one force chain contact experiencing frustrated rotation. At the global level, the MFMC encapsulates interconnections between force chains. The MFMC can be used to predict most of the force chain particles without need for any information on contact forces, thereby suggesting the network flow framework may have potential broad utility in the modeling of force transmission in unbonded and bonded granular media.

DOI: 10.1103/PhysRevE.91.062204 PACS number(s): 45.70.−n

I. INTRODUCTION

Not all contacts in a granular material are created equal. Previous studies have shown that forces in a deforming dense granular material are transmitted through a dual network of strong versus weak contacts [1,2]. The earliest demonstrations of this duality came from experiments that exploited birefringence patterns in particles made of photoelastic materials [3–5], a strategy that was used to deliver the first physical measurements of individual contact forces [2]. These studies of granular deformation in two-dimensions (2D) were pivotal in uncovering the underlying process of self-organization at the mesoscopic level. Self-organization is intimately tied to force transmission and is similarly dual in nature: Strong load-bearing columnar structures known as force chains continually form and persist to varying degrees depending on the lateral support provided by their weakly loaded neighbors [6–9]. Force chain columns, aligned in the direction of the major (most compressive) principal stress, are axially loaded and prone to failure by buckling [10]. The evolution of these confined columnar structures directly governs mechanical function at the macroscale, specifically, the load-bearing capacity and failure of the material [7–16]. Indeed, regardless of failure mode, diffused versus localized, the collective failure of force chains by buckling precipitates and controls global failure [12,14,17]. Detailed knowledge of the evolution of force chains and their confining weak neighbors, in 2D and 3D, is thus crucial for developing robust constitutive models that can adequately describe the deformation of many everyday granular materials (e.g., sand, rocks, ceramics, powders, and grains) [11,15,18–21]. Although significant attention has been paid to force transmission in granular systems, little is known about the regulation of internal forces that leads to this dual pattern of heterogeneity, in particular, its dependence on the strength of the contacts as well as the local and global topology of the contact network of the material (e.g., Ref. [11,21–26]). This gap in knowledge has become one of the most pressing issues in the science of granular materials, no doubt pushed to the forefront by the rapid advances in imaging techniques [21,27–34]. With unprecedented access to the grain scale and the ability to "see" inside a deforming granular material, we are now witnessing prodigious and complex data being generated on microstructural fabric (i.e., arrangement of grains and pores) for a wide range of spatial scales (e.g., Refs. [21,27–29]). This trend, coupled with the extant literature on the influence of microstructural fabric on mechanical response (e.g., Refs. [6,15,20,35]), provides clear impetus for new concepts and analytical tools that can harness and leverage the information embodied in these data sets and uncover patterns which facilitate an understanding of how microscale mechanisms (the cause) relate to macroscale performance (the effect). Accordingly, the aim of this study is to develop a model that can be used to establish a clear mechanistic link between these two scales, with the aid of data on microstructural fabric. Of specific interest is whether this model can identify the main structural elements in force transmission and uncover details

1539-3755/2015/91(6)/062204(14)

of intra- and interelement interactions, which may in turn yield insights into their functionalities.

We adopt a strategy that has been inspired by developments in complex systems, where heterogeneities in transmission patterns have yielded vital clues to the interdependencies between structure and functionality. Consider, for example, how Google ranks web pages on the Internet for search. Web pages are interconnected by hyperlinks, each carrying different levels of traffic. Various network-based algorithms can rank the pages and/or links by the level of traffic they support, thereby measuring their relative importance in the system hierarchy [36]. Google's PageRank [37] algorithm is one example. Now suppose that we can map out the grains in a deforming sand sample into networks, each representing the sample at each equilibrium stage of the loading history. The question then arises: Does the abstraction of individual grains and their contacts to a network facilitate the development of algorithms and models which operate in a similar manner to how PageRank finds important web pages, identifying particles in key mesoscale structural elements like force chains by searching a force network Internet? Here we formulate a general framework for developing models that can identify the major force pathways, including force chains, based on a network constructed from data on microstructural fabric (e.g., contact topology).

With respect to network representations of granular materials, past studies have demonstrated the efficacy of complex network techniques in unraveling the interdependencies between functionality and structure; see, for example, Refs. [18,24,38–42] and references cited therein. By far the most studied is the *contact network* where the nodes represent the grains and edges represent the interparticle contacts. As such, the study of force transmission through this contact network as a "network flow problem" is a natural next step. Broadly speaking, many real-world transmission phenomena, especially in industry, have been successfully modelled as a network flow problem involving a weighted, directed network [43–45]. In these settings, a given product or information is transported from a source node (origin) to a sink node (destination) through a network of intermediate nodes that are connected by edges (or arcs). Three prime examples in industry are transportation, communication, and water resources [43,44]. The commodity here may be cars, messages, and water, respectively; the corresponding nodes and edges may be intersections connected by streets, communication centers connected by communication channels, and water reservoirs or pumping stations connected by pipelines. Somewhat surprisingly, while network flow theory seems a natural framework for modeling force transmission in granular media, its application in granular rheology is largely unexplored. To the best of our knowledge, the first attempts at modeling force transmission patterns in granular media within a network flow framework are those in Refs. [46–49]. In Ref. [48], force transmission was analyzed as a network flow optimization problem using the concept of maximum flow–minimum cost (MFMC) in 2D discrete element (DEM) simulations. Guided by the lessons learned in Ref. [48], we now explore force transmission more deeply and for cohesionless and cohesive granular materials in 2D and 3D, based on measurable information on the local and global topology of the contact network and contact properties (e.g., bond strength). In particular, we test the hypothesis that the particles that form the contacts in the MFMC—namely those contacts in the percolating network that transmit the "maximum flow" (i.e., the highest units of force) at "minimum cost" (i.e., the least dissipated energy from such transmission)—comprise those in the main structural elements of force transmission. Primarily these elements are the columnar force chains and their laterally supporting neighbors in conjoined trusslike configurations [38]. It follows from this hypothesis that the transmission of force through the percolating MFMC must embody *intra*- as well as *inter*element interactions, i.e., between particles in individual force chains and their confining supports and between different force chains, respectively. To this end, we construct a network flow model of force transmission for two types of granular systems: (I) crushable agglomerate models of individual silica sand grains subjected to uniaxial compression [28] and (II) assemblies of photoelastic circular disks subjected to biaxial compression [50]. The data in (I) pertain to the prefracture regime with the exception of one data set which comprises measurements taken over many stages of the test well into the postfracture regime. Like (I), the data from the physical test in (II) include information on contacts as well as contact forces, a necessary information for establishing whether the MFMC can be employed to predict force chains. The stark differences in the evolution of the contact network of Systems (I) and (II) have important implications for force transmission, above and beyond those arising from loading conditions, material properties, and dimensionality. In a deforming granular material, forces at contacts undergo continual reconfigurations. Consequently, the force chain membership (i.e., which particles belong to force chains) is likewise subject to perpetual change. In (I), the force reconfigurations prior to fracture ensue over an almost invariant contact network, whereas those in (II) are coupled with the evolution of the contact network.

The paper is organized as follows. The physical underpinnings of the proposed network flow model and the key components of the MFMC are presented in Sec. II. In Sec. III, we present the data sets examined. We formulate the network flow model in Sec. IV before presenting our results in Sec. V. A summary of key findings and future related research is given in Sec. VI.

II. MAXIMUM FLOW–MINIMUM COST

To understand the motive and objective of this study, consider the key components of the MFMC [43,44]. The MFMC problem for transmission of a product through a network is solved for a given set of capacity and cost assigned to each edge. The former is an upper limit on the total number of product units that can pass, while the latter is a cost associated with the passage of one product unit, through the edge. The transmission of force through the grain contacts invariably involves energy dissipation that may be envisaged as an associated cost. Accordingly, we prescribe (i) a force-bearing capacity that represents the maximum force that can be transmitted through the contact and (ii) a cost that reflects the energy dissipated per unit of force transmitted at such contact. In this context, the solution to the MFMC problem, referred to hereafter as simply “MFMC,” consists of a percolating subset of contacts that transmit the maximum possible units of force with least energy dissipation. More specifically, we can think of the MFMC as a percolating subnetwork of major load-bearing pathways, which favor the most stable and shortest routes through the contact network in the given direction of flow (e.g., the most compressive principal stress). Clearly, the more stable the contact, the higher the force that it can support and transmit. As shown in past studies, notably that of Wolf *et al.* [51], energy dissipation is least along these major pathways. Sliding friction, the major contributor to energy dissipation, is essentially confined to the complementary weak contact network. While energy dissipation may arise from rolling friction, this is much less for systems comprising idealized shaped particles such as those examined here. Moreover, energy dissipation through rolling friction generally occurs in a collapsing (buckling) force chain, when member particles have weakened and ceased to be a major load bearer. Stability is not the only factor governing MFMC. To minimize cost, more direct or shortest routes through the contact network are also important, which explains why quasilinear structural building blocks of force chains are likely to be part of MFMC when considering force transmission in the direction of the most compressive principal stress.

The intended application of MFMC is also crucial in the formulation of the capacity and cost functions. For the purposes of identifying the major load-bearing pathways in a system, what matters are the relative values and not the actual values of the capacities and costs for the constituent contacts. Hence, these functions can be based on qualitative proxy measures rather than quantitative measures of force-bearing capacity and energy dissipation. If, on the other hand, the intent is to use MFMC to establish the actual values of the forces transmitted through the different contacts, then the capacity and cost functions must accurately quantify the force-bearing capacity and energy dissipation at the contacts. This study is focused on the former; the latter application is outside the scope of the present analysis.

In light of the factors discussed above, we can now build on Ref. [48] and the available information on microstructural fabric from high-resolution measurements. In Ref. [48], a uniform capacity function was used, coupled with a ternary cost function to represent the different modes of contact (0 for an elastic stick contact, 1 for plastic sliding or plastic rolling, and 2 for a plastic contact that is undergoing both sliding and rolling). In that case, the MFMC pathways represent percolating shortest routes through the network—in favor of the stable elastic contacts as opposed to the unstable plastic contacts where relative sliding and/or rolling occurs. While the results proved promising, the study in Ref. [48] also prompted a need to explore capacity and cost functions that more closely reflect reality from two perspectives: (i) the contact strength governed by resistances to relative motion at the contacts and (ii) *both* the local as well as global topology of the contact network. The capacity function depends on factors that govern the contact strength (e.g., bond strength, contact area, friction, etc.) For bonded granular systems well into the fracture regime, we expect the strength of the bonded contacts and the frictional properties of the unbonded contacts to both contribute to the capacity function. On the other hand, the cost function that describes the energy dissipation associated with the transmission of force may depend on the local contact topology. The dependence of energy dissipation on the local contact topology is best understood from the perspective of structural stability. Recent studies have shown that certain local contact topologies, in particular, the 3-cycles (i.e., three grains arranged in mutual contact), effectively act like triangular trusses with respect to force chain columns. The 3-cycles brace the force chain columns both to increase rigidity where needed (i.e., by propping-up column misalignments) and to frustrate relative grain rotations that constitute the precursory mechanism for force chain failure by buckling [24,38,39]. As shown in recent simulations and physical experiments, the higher the number of 3-cycles that constituent contacts are part of, the more stable are these contacts [38]—and in turn the overall material [9,38–41]. We therefore expect the dissipated energy per unit of force transmitted to be less for a stable-overconstrained contact when compared with that for an unstable-underconstrained contact. This is because significant relative motions (i.e., sliding and rolling) and contact breakage can rapidly occur in the latter, due to lack of local support and rolling resistance at the contact. Corroborative evidence, recently uncovered by tracking the local contact cycle topology of individual grains throughout loading history, showed a strong correlation between the change in the contact cycle topology and measures of the fluctuating kinetic energy and energy dissipation at both the local and global levels [52]. That microstructural (here contact) information alone can be used as a proxy for energy dissipation bears merit, since contacts can now be identified and tracked throughout loading history, even for sand using synchrotron microcomputed tomography [27,28]. Indeed, structural proxy measures for force and energy dissipation are helpful in advancing the state of knowledge on the transmission of force in 3D systems since contact forces have proven to be difficult to reliably capture, especially over many stages of a test under combined compression and shear [27,28,32]. Multiple advanced experimental techniques such as confocal microscopy [30], micro-CT scanning [31,34], refractive index-matching tomography [21], and neutron imaging [33] have been applied to overcome this challenge. While promising, these approaches are limited in the systems they can be applied to. For example, index matching only can be used on materials with very specific optical properties, and neutron imaging is too computationally intensive to be used with systems larger than a few hundred grains.

III. DATA

We examine two systems, (I) and (II), both of which have been reported in the literature [28,50]. For completeness, we summarize the salient aspects of these systems below, providing more information for (I) since the evolution of the microstructural fabric of these agglomerates has only been partially studied [28], whereas that of (II) has been comprehensively characterized in Refs. [9,50].

A. System (I)

System (I) consists of crushable agglomerate models of individual silica sand grains subjected to uniaxial compression

TABLE I. System (I). The four agglomerates A–D vary in size, bond strength, and macroscopic response as measured by the peak load (i.e., the highest load experienced before fracture). No obvious trends in peak load are observed: Both A and D are weaker than B and C despite having lesser and greater numbers of particles, respectively, and B and C have a similar peak load but very different bond strengths.

Agglomerate	Number of particles	Bond strength (MPa)	Peak load (N)
A	263	500	54
B	358	510	108
C	355	402	110
D	501	454	87

[28]. The DEM simulations, performed using PFC3D [53], were developed to faithfully represent experimental measurements using synchrotron micro-tomography to acquire *in situ* three-dimensional (3D) images of silica sand grains. Each grain was represented by a crushable agglomerate composed of small spherical particles whose radii vary between $R_{\min}$ and $1.2R_{\min}$, where $R_{\min} = 0.035$ mm. The particles are linked by parallel bonds, in accordance with the bonded particle model (BMP) proposed by Potyondy and Cundall [53]. The parallel bond acts over a circular cross section on the contact plane of two bonded particles. This bond can resist force and moment and hold two contacting particles together up to a predefined limit referred to as the bond strength. Each agglomerate is assigned a bond strength, which is chosen randomly from a distribution determined from experimental observations of silica sand grains. This distribution has a mean strength of 475 MPa and standard deviation of 150 MPa. The same values for the bond strength were used for both tensile and shear stresses. Particles overlap at contact points (soft-contact approach). The region of overlap is negligibly small compared to the particle dimensions and is proportional to the contact force. The interaction of particles at contacts is governed by a linear contact spring-slider model which permits sliding behavior. If a parallel bond is added to the contact, the linear contact model and parallel bond act in parallel. If the tensile (normal) or shear stress within the bond material exceeds its assigned limit, the parallel bond breaks and is removed from the system. The linear contact model becomes active if the two particles are still in contact. Each agglomerate is compressed between two rigid platens at a constant velocity and the evolution of the properties of particle contacts are tracked throughout the loading history. To achieve the desired match to the mechanical and physical behavior of silica sand grains, the minimum diameter of spherical subparticles, the bond strength between spherical subparticles, and the overall shape and fabric of the agglomerates were altered in 40 different DEM simulations. We study four agglomerates from these simulations. Although full details are in Cil and Alshibli [28], we summarize their properties and macroscopic response in Table I and discuss briefly below their internal fabric and force distributions.

Data for Systems A, B, and D cover the prefracture regime only; data for System C extend to the postfracture regime. Differences in the internal contact force regulation across the agglomerates manifest in the mechanical response at the macroscopic level: see peak load values in Table I. There are two main factors behind these differences. First, each agglomerate has its own unique initial microstructural fabric as evident in the distributions of internal connectivity [Fig. 1 (left)], in addition to the number of constituent particles. This fabric was achieved by generating at random nonuniformly sized spherical particles inside an encapsulating spherical shell and then subjecting this assembly to a low isotropic compression by uniform expansion of constituent particles (radii increased uniformly). Second, complex interactions occur between each agglomerate and the loading platens. In the initial stages of compression, the agglomerate may rotate and translate to attain a more stable configuration (e.g., achieved at around stage 150 for agglomerate A) based on agglomerate morphology and orientation. The resultant contact region may also effect the subsequent deformation: in some cases, a single subsphere may be in contact with the loading platen while in others multiple subspheres may be involved.

Despite the quantitative differences noted above, there are commonalities and qualitatively similar trends in the agglomerates' response to crushing. In all cases, the percentage of particles in force chains undergo small fluctuations about an essentially constant value [i.e., average values are 13% (A), 16% (B), 14% (C), and 18% (D)], though the size of these fluctuations increases during breakage events [Fig. 1 (top right)]. No correlation between the contact forces and the distribution of the contacts was observed. In all the agglomerates, the major force pathways are generally aligned in the direction of compression as shown in Figs. 1 (bottom right) and 2(d). In the Lambert projection in Fig. 1 (left), these major force pathways would be situated at the center and in the closely spaced circles close to the periphery: that part of the grain agglomerate in contact with the top and bottom platens, respectively. From Fig. 1 (left), we see these are not consistently coincident with the regions of high connectivity (red zones). Finally, despite the continual force reconfigurations inside each agglomerate during crushing, as first reported in Ref. [28], the average number of contacts per particle in force chains is essentially invariant prior to fracture: We observe an average of six (five) contacts per particle in force chains (non force chains) across all agglomerates A–D.

B. System (II)

System (II) is from a 2D experiment involving an assembly of unbonded photoelastic disks subjected to biaxial shear strain [13,50]. Briefly, collections of roughly 1500 bidisperse particles, here circular disks, rested on a smooth horizontal Plexiglas sheet. A rectangular structure bounded the particles horizontally, and the spacing between opposing pairs of walls in the boundary were driven to produce pure shear, here compression in one direction applied at constant velocity, expansion in the other, all at fixed area. The procedure that was first reported in Ref. [2] was used to determine the contacts among the particles, and the vector values of the forces at contacts. This allowed details of the contact and force networks and the evolution of these networks to be tracked under shear strain. This experiment is discussed in great detail in Ref. [50]. The evolution of microstructure for this system with respect to

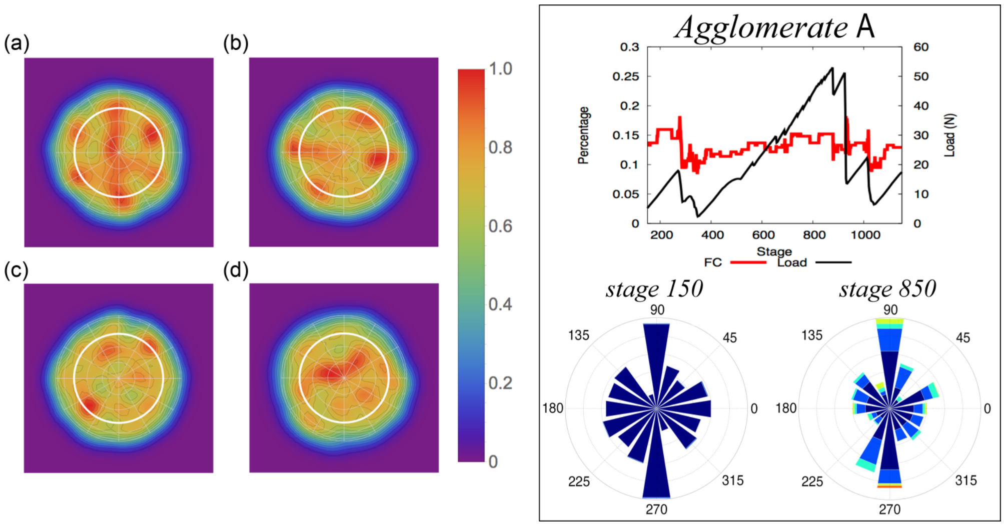

FIG. 1. (Color online) System (I): The microstructural fabric of agglomerates A–D is shown by their initial interparticle contact density distribution (left). Each image shows the full surface of a unit sphere in the Lambert projection [54]. Thin white radial lines from the center mark equal 30° increments of "longitude" from 0° to 360°. White concentric circles mark 30° increments of "latitude" from 0° (top of the agglomerate) to 180° (bottom of the agglomerate); the thick white circle shows the "equator" at 90° latitude, and circles become closer towards the bottom of the sphere. System (I)A: Evolution of the compressive load and the percentage of particles in force chains (FC) (top right); polar plots of normalized compressive contact forces (bottom right; color bar used is the same as that for contact densities on left). Similar evolution trends apply to B–D.

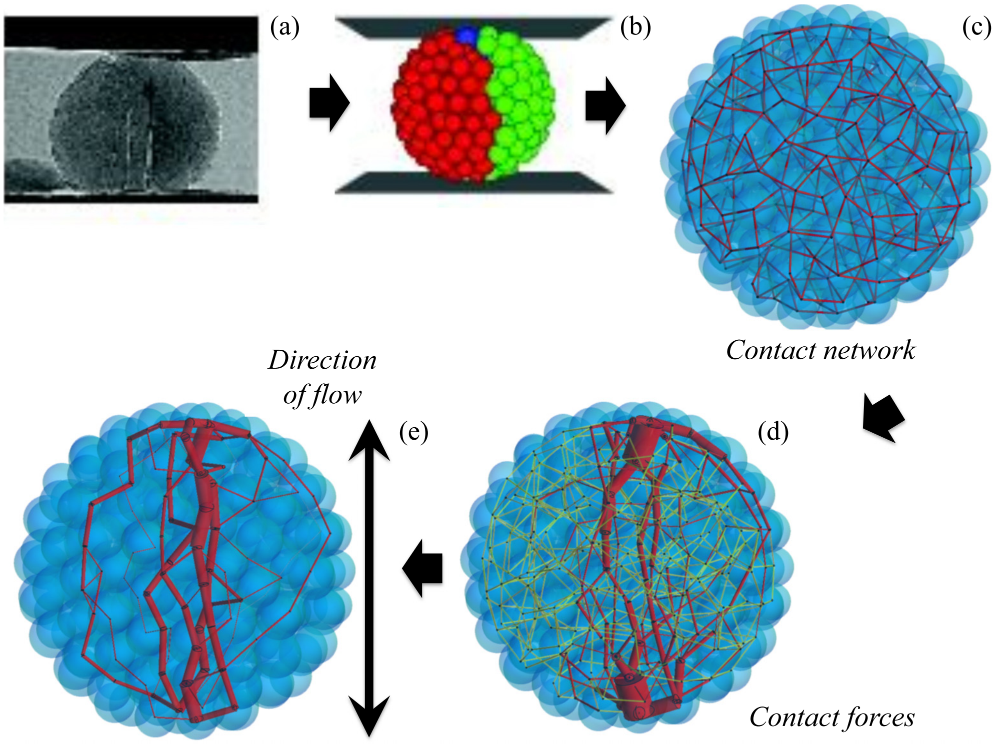

FIG. 2. (Color online) The key components of the proposed analysis of force transmission at each stage of the crushing test for a sand grain prior to fracture. (a) The sand grain and (b) its associated agglomerate model comprising bonded subspheres. (c) The contact network and (d) the associated contact force distribution. In (d), the contacts transmitting normal contact forces greater than (less than or equal to) the global average are shown in red (yellow) [in black and white, dark grey of varying thickness and light grey of constant thickness respectively]; line thickness represents the magnitude of the normal contact force transmitted. This concentration of major force pathways along the central axis of the grain agglomerate, in alignment with the direction of compression, is representative of force transmission patterns across all the agglomerate models. (e) The MFMC flow network model with the line thickness representing the flow transmitted at the contacts.

the structural building blocks of force chains and supporting n cycles has been fully characterized in Ref. [9].

IV. THE NETWORK FLOW MODEL

We model force transmission in a granular material which is compressed in the vertical direction between two parallel walls (top and bottom loading platens) at a constant velocity. Figure 2 provides a depiction of the different parts of this analysis in a crushing test of a silica sand grain. We formulate our model as a network flow optimization problem [43,44]. This involves the construction of a flow network $\mathcal{N} = (s,t,V,E,U,C)$, where

(i) s and t are two artificial nodes called the source and sink, respectively, such that flow can be sent from the source node s to the sink node t. These nodes can be used to represent the top and bottom loading platens through which the material is compressed. By virtue of Newton's third law, the flow of force along each edge is symmetric (i.e., equal and opposite forces act at each contact): This means that the flow from the source to the sink is the same regardless of which loading platen acts as the source versus the sink.

(ii) V is the set of intermediate nodes that represent the particles.

(iii) E is the set of edges, connecting nodes in V, that represent the contacts between particles.

(iv) $U = \{u_{(i,j)} : (i,j) \in E\}$ is the set of capacities of the edges. For each edge $(i,j) \in E$, the element $u_{(i,j)}$ represents the maximum amount of flow (force) that can be transmitted through the edge (i,j).

(v) $C = \{c_{(i,j)} : (i,j) \in E\}$ is the set of costs associated with the edges of the network $\mathcal{N}$. For each edge $(i,j) \in E, c_{(i,j)}$ represents the cost of sending one unit of flow through the edge (i,j).

The problem of transmitting the maximum units of force with minimum dissipated energy through the material can be formulated as the MFMC problem for the network $\mathcal{N}$. We solve this problem in two steps:

(a) find the maximum flow $|f|^*$ through the flow network from source s to sink t using the Ford-Fulkerson algorithm [55] and

(b) distribute the maximum flow $|f|^*$ through the network $\mathcal{N}$ such that the total cost is minimized subject to the following constraints on the flow $f_{(i,j)}$:

(i) Capacity constraint: $f_{(i,j)} \leqslant u_{(i,j)}, \forall (i,j) \in E$, where the edge weight $w_{(i,j)}$ is set equal to the capacity, $w_{(i,j)} = u_{(i,j)}$. The flow $f_{(i,j)}$ cannot exceed the edge capacity $u_{(i,j)}$.

(ii) Conservation of flow: $\sum_{m\in V} f_{(m,p)} = \sum_{n\in V} f_{(p,n)}, p \neq \{s,t\}$. The net flow entering a node is the same as that exiting that node, except for the source or sink.

(iii) The total flow leaving the source node s must equal that entering the sink node t: $\sum_{m\in V} f_{(s,m)} = \sum_{m\in V} f_{(m,t)}$.

The solution to the MFMC problem, coined earlier as MFMC, is a subset of edges in $\mathcal{N}$ [56]. For the systems studied here, the MFMC represents a percolating subnetwork in the global contact network of the material: see Fig. 2(e). We illustrate the operation of the MFMC algorithm with the aid of simple toy model in Fig. 3. It is useful to note the following three special cases of the MFMC problem. First, if all costs are set to zero, the MFMC problem is equivalent to finding the maximum flow through the network. Second, if $|f|^*$ is a solution of the maximum flow with capacities $u_{(i,j)}$, then $\gamma\, |f|^*$ is a solution with new capacities $\gamma\, u_{(i,j)}$, where $\gamma > 0$ is a constant; the solution to the maximum flow problem depends on the relative values of the capacities, not the actual values. Third, the solution to the MFMC problem with costs $c_{(i,j)}$ is the same as that with costs $\gamma\, c_{(i,j)}$, where $\gamma > 0$ is a given constant (the total cost will be increased by a factor γ, without affecting the flow distribution).

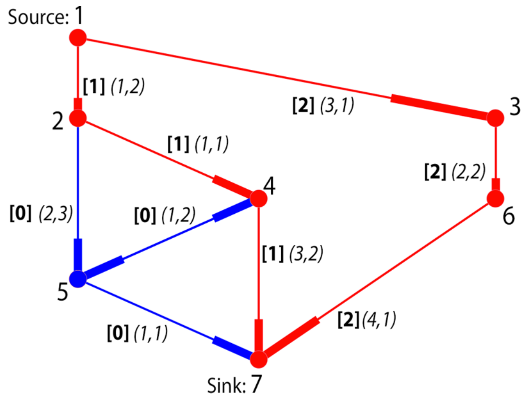

FIG. 3. (Color online) A toy model, involving a seven-node flow network, to explain the essence of the maximum flow–minimum cost (MFMC) algorithm. Node 1(7) is the source (sink). Next to each edge (i,j) is $[f_{(i,j)}]$ $(u_{(i,j)}, c_{(i,j)})$. Thick lines next to a node encode the edge direction, i.e., the "end" of the flow [e.g., nodes 3 and 6 is connected by edge (3,6) transmitting flow that starts at 3 and ends at 6, whereas nodes 4 and 5 have two edges (4,5) and (5,4)]. Now consider each path from source 1 to sink 7. The right-hand path (1-3, 3-6, 6-7) is the simplest. Of the edges in this path, 3-6 has the lowest capacity of 2 (3-6 is the bottleneck). Therefore, a maximum 2 units of flow can be sent along this path, for a total cost of $2 \times (1 + 2 + 1) = 8$ (i.e., the total flow multiplied by the sum of edge costs). The left-hand path is more complex. Again, we have a bottleneck at 1-2, allowing only 1 unit of flow to pass from source to sink at a cost of 2. From node 2, multiple routes are possible: (2-4, 4-7), (2-5, 5-7), (2-4, 4-5, 5-7), and (2-5, 5-4, 4-7). The costs of these are 3, 4, 4, and 7, respectively. With (2-4, 4-7) having the lowest cost, the left-hand path is thus (1-2, 2-4, 4-7). We now have the complete MFMC pathway, made up of the edges (1-3, 3-6, 6-7, 1-2, 2-4, 4-7). This MFMC pathway carries 3 units of flow for a total cost of 13.

We construct a total of four MFMC models, each involving a particular pair of capacity and cost functions. We chose these functions to be as simple as possible, while embodying the most critical factors that govern force transmission at the local or particle level (i.e., local contact topology and bond strengths) in addition to the global contact topology of the material that is embodied in the flow network. Of key interest in this study are (i) the force chain capture rate of MFMC for each model, i.e., the fraction of particles in columnar force chains that form the MFMC contact network; (ii) the composition of the MFMC in terms of the strong versus weak contacts; and (iii) the extent to which the weak contacts in the MFMC provide direct support to force chains and their associated configurations relative to the force chains they support. In what follows, we introduce the capacity and cost functions employed in the four MFMC models.

A. Capacity functions

1. *Uniform capacity function*

For a baseline model, we prescribe a uniform capacity for all edges (i,j):

$$u_{(i,j)} \triangleq \begin{cases} \infty, & \text{if } i = s \text{ or } j = t \\ 1, & \text{otherwise.} \end{cases} \tag{1}$$

2. *Capacity function based on breakage criterion*

Here we propose a capacity that is based on the contact model used in the agglomerate models [28]. These models adopted the bonded particle model (BPM) of Potyondy and Cundall [53], in which the contacts are joined by a bond that can sustain tensile and shear stresses up to prescribed bond strengths, $\bar{\sigma}_{(i,j)}$ and $\bar{\tau}_{(i,j)}$, respectively. These strengths were set equal to a single bond strength $S_{(i,j)}$ in Ref. [28]: Recall also Table I. Bonds carry both force and moment ($\bar{F}$ and $\bar{M}$, respectively), which can be resolved into normal and shear components with respect to the contact plane ($\bar{F}^n, \bar{F}^s, \bar{M}^n, \bar{M}^s$). The maximum tensile and shear stresses acting on the bond are given by

$$\sigma^{\max} = \frac{\bar{F}^n}{A} + \frac{|\bar{M}^s|\bar{R}}{I}, \tag{2}$$

$$\tau^{\max} = \frac{|\bar{F}^s|}{A} + \frac{|\bar{M}^n|\bar{R}}{J}, \tag{3}$$

where I and J are the moment of inertia and polar moment of inertia, respectively. The bond area is $A = \pi \bar{R}^2$, where $\bar{R}$ is the bond radius given by

$$\bar{R} = \lambda \ \min(R_i, R_j); \tag{4}$$

here λ is a constant multiplier and $\min(R_i, R_j)$ is the smaller of the two radii of the contacting particles i and j, R_i and R_j. Recall from Sec. III that the particles' radii lie in the range $R_{\min}$–$1.2R_{\min}$, where $R_{\min} = 0.035$ mm. If either the normal or shear stress exceeds the bond strength $S_{(i,j)}$, then the bond is considered broken. Neglecting the moment term in both stresses (which are much lower than the force terms in these agglomerates) leads to a critical threshold force $F_{(i,j)}$ for each bond, $S_{(i,j)} = \frac{F_{(i,j)}}{A}$. This leads to the following load-bearing capacity of a bonded contact between particles i and j:

$$u_{(i,j)} \triangleq \begin{cases} \infty, & \text{if } \ i = s \text{ or } j = t \\ F_{(i,j)} = A\ S_{(i,j)} = \pi\ S_{(i,j)}\ \bar{R}^2, & \text{otherwise.} \end{cases} \tag{5}$$

B. Cost functions

1. *Uniform cost function*

This is the simplest cost function in which all edges are assigned identical costs:

$$c_{(i,j)} = 1. \tag{6}$$

2. *Cost determined by the local 3-cycle topology*

A more physically relevant cost function is one governed by the 3-cycle membership of the contact (i.e., the number of 3-cycles that include the edge). Possible values are 0, 1, or 2:

$$c_{(i,j)} \triangleq \begin{cases} 0, & \text{if the edge is a member of 2 or more 3-cycles} \\ 1, & \text{if the edge is a member of one 3-cycle} \\ 2, & \text{if the edge is not a member of any 3-cycles.} \end{cases} \tag{7}$$

3. *Cost determined by the local 4-cycle topology*

Analogous to Eq. (7), we can similarly propose a cost function that is based on the 4-cycle membership of the contact:

$$c_{(i,j)} \triangleq \begin{cases} 0, & \text{if the edge is a member of 2 or more 4-cycles} \\ 1, & \text{if the edge is a member of one 4-cycle} \\ 2, & \text{if the edge is not a member of any 4-cycles.} \end{cases} \tag{8}$$

Since 4-cycles do not provide the same level of resistance to force chains as 3-cycles (see, for example, Ref. [38]), we expect the capture rate of MFMC for this cost function to be less than that from Eq. (7) for the same capacity function.

4. *Cost determined by the average clustering coefficients of the particles in contact*

The cost function can be expressed in terms of the network node property known as clustering coefficient:

$$c_{(i,j)} \triangleq 1 - \tfrac{1}{2}(C_i + C_j); \tag{9}$$

here C_i is the clustering coefficient of node i, defined as the ratio of the number of 3-cycles that the node is part of, T_i, to the maximum number of 3-cycles that the node could be part of given its degree k (i.e., number of edges) [44],

$$C_i = \frac{T_i}{k_i(k_i - 1)}. \tag{10}$$

Thus higher edge clustering values are assigned lower costs. We expect the capture rate of MFMC to be comparable to that obtained from 7 for the same capacity function.

From the cost and capacity functions described above, we construct four different network flow models. These are summarized in Table II. Model 1 uses a uniform capacity and cost function, the most basic model possible. Models 2–4 all use the breakage criterion capacity function for the unbonded system (I), paired with the remaining cost functions as described above. The *input information* to each network flow model is as follows: the bond strengths and the particle contacts for System (I) and the particle contacts for System (II). To assess the predictive capacity of each model, the following data are needed: (i) contact forces to identify the contacts

TABLE II. System (I): All four models are implemented in agglomerates A–D. System (II): A hybrid of model 1 and model 2 is adopted, i.e., uniform capacity and a cost function determined from 3-cycle membership.

Model	Capacity	Cost
1	Uniform	Uniform
2	Breakage criterion	3-cycle topology
3	Breakage criterion	4-cycle topology
4	Breakage criterion	Clustering coefficient

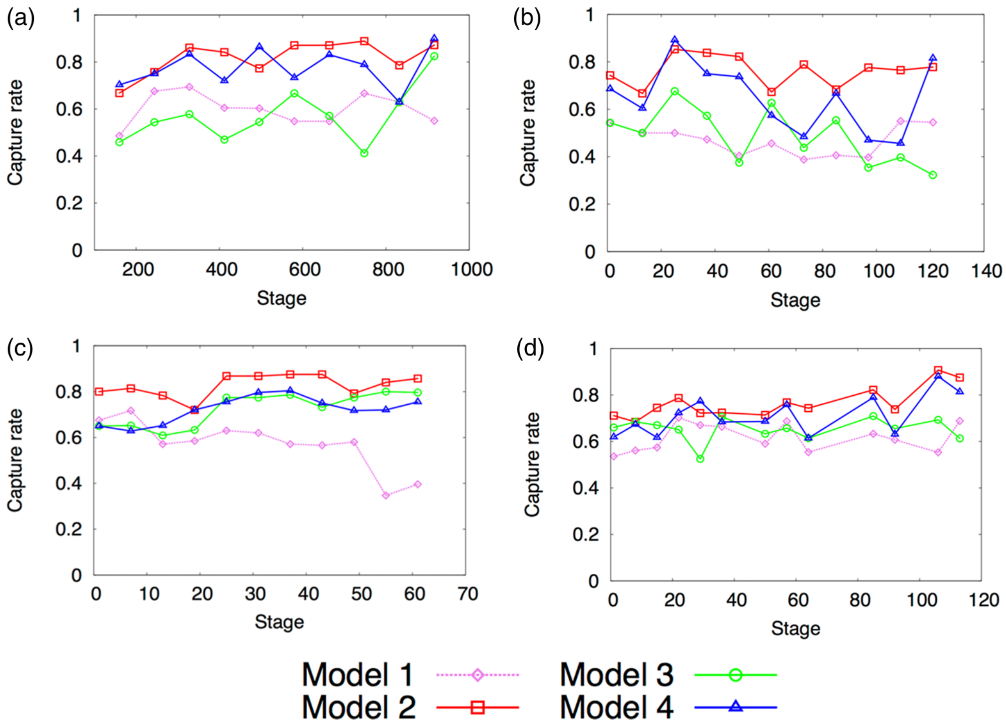

FIG. 4. (Color online) System (I): The relative performances of models 1–4 based on their capture rate. Model 2 (capacity: breakage criterion; cost: 3-cycle membership) performs the best of all four models, followed by model 4 (capacity: breakage criterion; cost: clustering).

belonging to the strong versus weak contact network and (ii) position and contacts of each member particle along with the contact forces to identify those particles in force chains, in accordance with the method in Refs. [57,58].

V. RESULTS

We present here the performance of the candidate MFMC models 1–4 for all four agglomerates A–D in System (I) before testing the best performing cost function together with a uniform capacity in System (II). Keeping in mind these network flow models do not require any information on contact forces for input, we assess performance based on each model's capture rate (i.e., the fraction of particles in force chains that form the MFMC contact network), where the force chains are determined using the method in Refs. [57,58]. Of interest also are the functional roles of the rest of the MFMC contacts that are not part of force chains. We will determine these by examining the composition of the MFMC with respect to the strong versus weak contacts. We note here that not all strong contacts are in force chains; the latter is a more stringent category requiring not only the transmission of relatively high contact forces that amount to an above average particle load vector but also a geometric alignment of these particle load vectors, consistent with the transmission of force along a particle column [57,58].

A. MFMC performance before grain fracture for System (I)

Before fracture, there is little gain or loss of grain contacts in the agglomerates. As such, the MFMC problem is solved on

TABLE III. System (I): The average capture rate of MFMC for all agglomerates A–D (column 3): the fraction of particles in major load-bearing force chains (FC) that form the MFMC contact network, averaged over all stages of loading prior to fracture. *Models are sorted in order of decreasing capture rate.* The composition of MFMC (columns 4 and 5): the average fraction of MFMC contacts that belong to the strong contact network (SCN) versus the weak contact network (WCN). Contacts in SCN (WCN) transmit above (at most) the global average contact force magnitude. Model 2 is the best-performing model, capturing the highest fraction of particles in FC (76–83%). The majority of MFMC contacts from model 2 (76–79%) are in the strong contact network (SCN).

Agglomerate	Model	FC	SCN	WCN
A	2	0.82	0.78	0.22
	4	0.76	0.80	0.20
	1	0.60	0.96	0.04
	3	0.57	0.67	0.33
B	2	0.76	0.76	0.24
	4	0.65	0.79	0.21
	3	0.49	0.71	0.29
	1	0.47	0.95	0.05
C	2	0.83	0.76	0.24
	4	0.73	0.70	0.30
	3	0.71	0.69	0.31
	1	0.57	0.95	0.05
D	2	0.76	0.79	0.21
	4	0.71	0.66	0.34
	3	0.65	0.67	0.33
	1	0.62	0.89	0.11

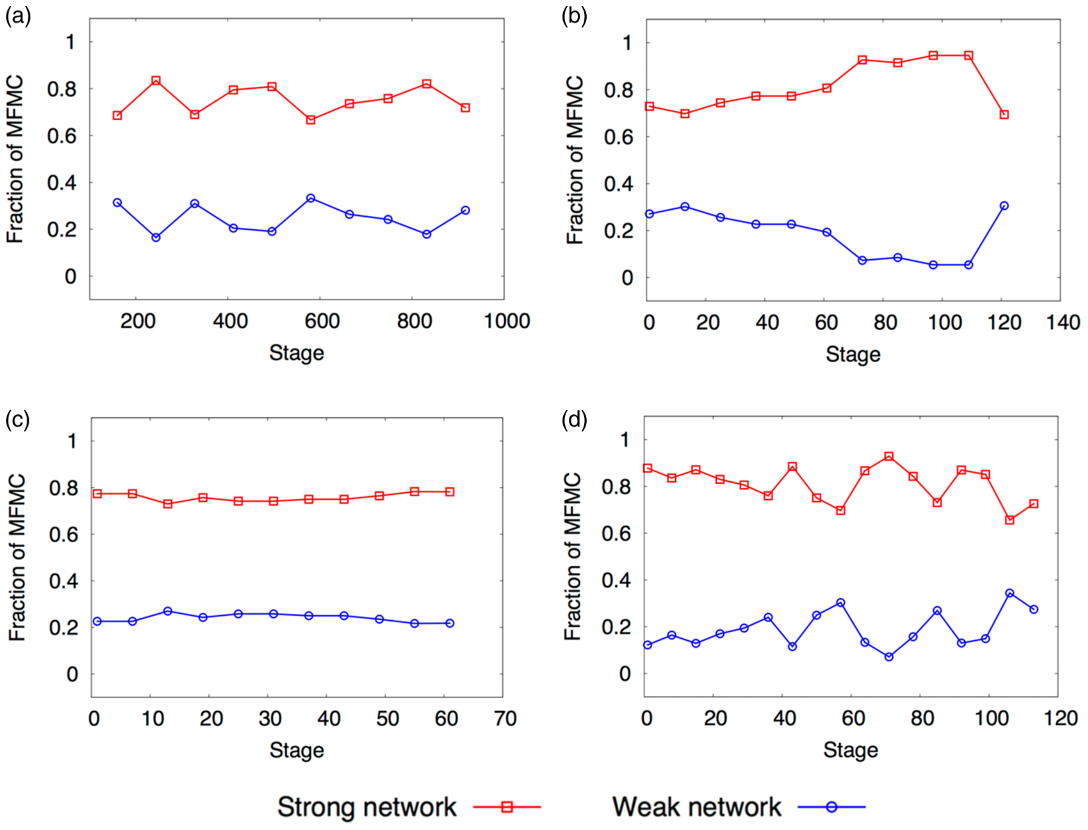

FIG. 5. (Color online) System (I): The composition of MFMC from model 2 with respect to the strong versus weak contact networks for all agglomerates A–D. The majority (above 75%) of the MFMC contacts are in the strong contact network.

an essentially fixed contact network. Recall from Fig. 2 that the major force pathways mainly concentrate along the central axis of the grain agglomerate, in alignment with the direction of compression. Figure 4 shows the performance of the candidate models 1–4 for all four agglomerates, quantified according to their capture rate. The fluctuations across the different stages of each test are indicative of the continual contact force reconfigurations that take place in the internal contacts of each agglomerate, as first reported in Ref. [28]. The best performing is model 2 (capacity from breakage criterion, cost from 3-cycle membership), on average capturing at least 76% of the force chain particles. Model 4 (capacity from breakage criterion, cost from clustering coefficient) also performs well in general.

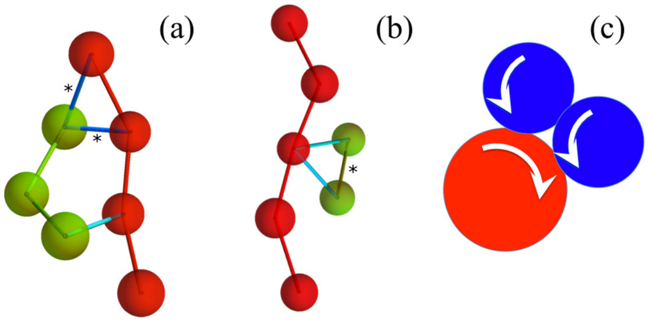

FIG. 6. (Color online) The great majority of the weak contacts in MFMC from model 2 are in 3-cycles that *directly* support a force chain through two configurational Modes I and II. Examples shown here are from System (I): (a) Mode I, two force chain particles are laterally supported by one confining neighbor through weak contacts (dark blue links, marked by asterisks), and (b) Mode II, one force chain particle is supported by two confining neighbors that interact through a weak contact (green edge, marked by an asterisk). (c) An example of particle rotations in Mode II where the force chain particle (red, light grey) is *not* subject to frustrated rotation from either of its confining neighbors (blue, dark grey). Most of the weak contacts in MFMC from model 2 of System (I) are in Mode I [83% (A), 89% (B), 90% (C), 87% (D)], where at least one force chain contact is subject to frustrated rotation.

Table III provides a summary of each model's capture rate. It is clear that model 2 is the best performing over all agglomerates, capturing the largest fraction of major load-bearing particles with respect to FC. We note that this finding is the same if model performance is instead judged according to the capture rates of particles in other subgroups of major load-bearing particles: particles with at least one contact transmitting above average contact force and particles bearing above the average particle load vector magnitude [58]. It is instructive to examine the MFMC contacts that are not part of force chains. These comprise strong and weak contacts. To elucidate the functional roles of these pathways, we examine the MFMC composition. A summary of this is given in the last two columns of Table III for all models, while Fig. 5 shows the evolution of the composition of the MFMC for the best performing model 2. At least 76% of MFMC contacts belong to the strong contact network, many of which are part of force chains. The great majority of the weak contacts in MFMC

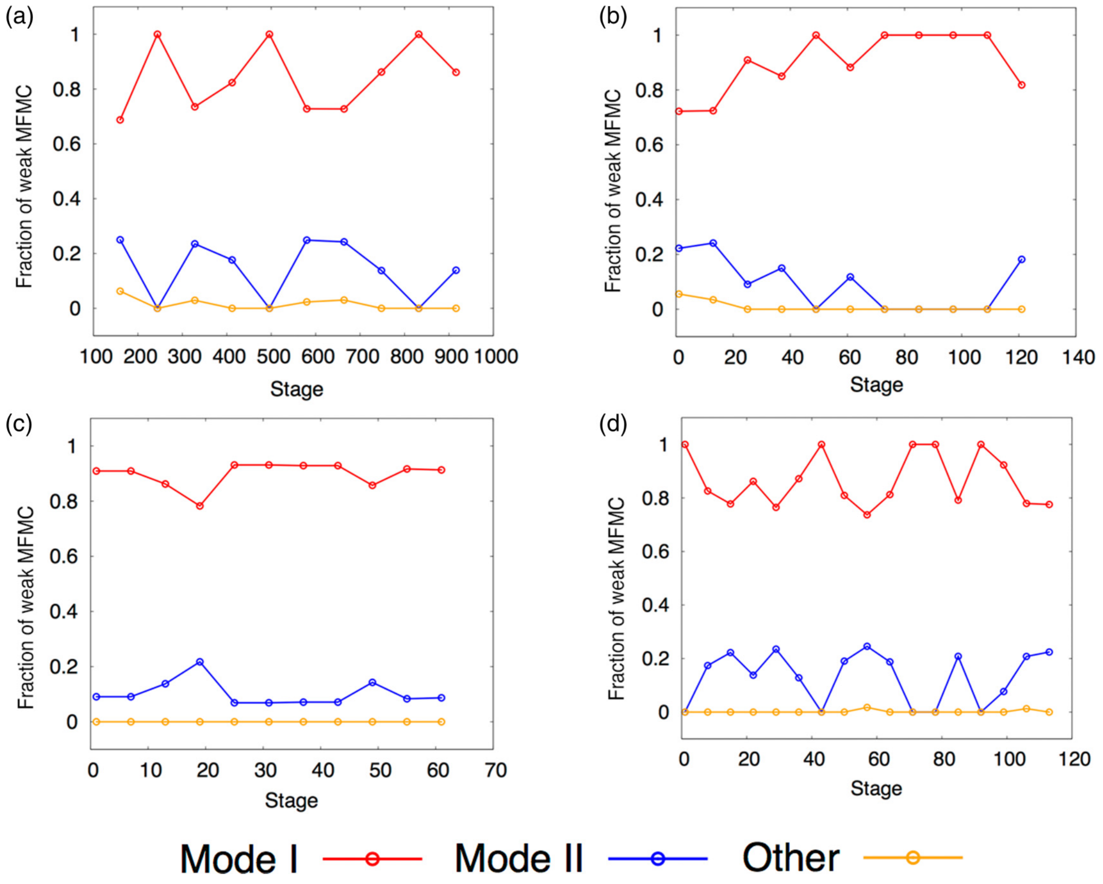

FIG. 7. (Color online) System (I). The evolution of the configurational mode in which weak MFMC contacts from model 2 belong for all agglomerates A–D. Essentially all weak MFMC contacts are in 3-cycles directly supporting a force chain particle. The great majority are in Mode I.

are in conjoined 3-cycles, i.e., those that *directly* support force chains (Fig. 6). Although to some extent this is to be expected given the cost function, there is a clear preference in the topology of these supports: most are in configurational Mode I (Figs. 6–7), consistent with an earlier finding on the preferred configuration of weak contacts around force chains in a cohesionless assembly of polyellipsoid particles under triaxial compression [17]. In Mode I [Fig. 6(a)], both frustration of rotation and lateral support are provided to two force chain particles by one confining neighbor. In this mode, at least one of the contacts with the force chain will be subject to frustrated rotation, regardless of the direction of rotations among member particles of the 3-cycle. In Mode II, it is possible for frustrated rotation to operate only at the contact between the confining neighbors, as depicted in Fig. 6(c). Thus, the MFMC consists mainly of the contacts in force chains and their supporting conjoined 3-cycles.

B. MFMC performance after grain fracture for System (I)

As previously mentioned, we focus our analysis of System (I) on force transmission in the prefracture regime, since the data for these agglomerates were confined to this regime [28], except for one agglomerate (System C) for which the simulation was undertaken well into the postfracture regime. Specifically, loading continued for System C after the agglomerate had split into two "daughter" fragments, fracturing parallel to the major and most compressive principal stress, as shown in the inset of Fig. 8. For completeness, we capitalize on this opportunity and test the capture rate of the best performing MFMC model 2 with respect to force chains in the postfracture regime.

After fracture, the contact network is no longer a single connected graph: Instead, multiple smaller contact networks arise corresponding to the daughter fragments. In this case, the MFMC problem is solved for the contact network of each of these daughter fragments. While the MFMC performs well on intact agglomerate systems, applying it to larger collections of agglomerates would require robust performance in the presence of large frictional rearrangements among fragments and continuing contact breakages among particles. From Fig. 8, it can be seen that the MFMC continues to capture the majority of force chain particles past the point of fracture, albeit the capture rate is smaller. This is to be expected as the capacity and cost functions that were used here were the same as those prior to the first fracture event, i.e., the capacity function does not distinguish between unbonded-frictional contacts versus bonded contacts. It may be possible to further improve the MFMC algorithm and maintain the high capture rates postfracture through improved capacity and cost functions that account for the progressive damage to the grain agglomerate (i.e., to explicitly handle new frictional unbonded contacts that come into existence as the agglomerate breaks up).

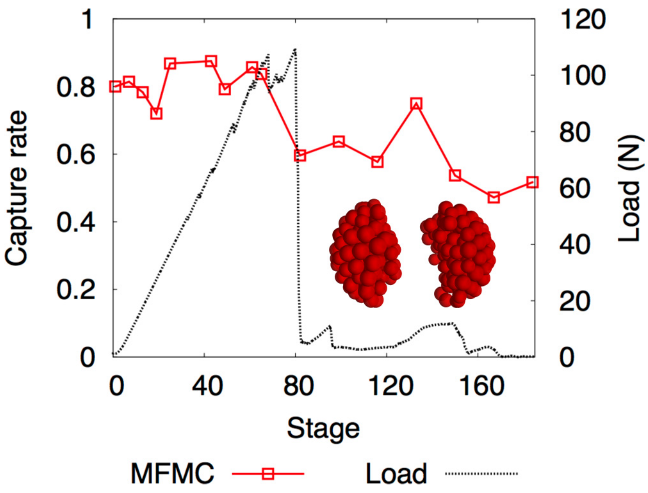

FIG. 8. (Color online) System (I): The evolution of the capture rate of MFMC from model 2 well into the fracture regime for agglomerate C. While the capture rate does decrease after the first major fracture event (fragments shown in inset), it maintains a capture rate of 60% or more until around stage 140. At this point, another fracture event occurs; the capture rate drops slightly though remains above 50%.

C. MFMC performance for System (II) and commonalities with System (I)

Given that the constituent particles of System (II) are made of the same material and there are no bonds at contacts, we adopt a uniform capacity function for this system. For the cost function, we adopt that of model 2, the best-performing model from System (I). As shown in Fig. 9, we found comparable capture rates as those observed for System (I). Similarly, almost all the weak contacts in MFMC (approximately 98%) are in conjoined 3-cycles that directly support force chains. Like those found in System (I), these are mostly arranged in one of two configurational modes, as depicted in Fig. 6. Mode I weak contacts comprise on average 79% (Fig. 9): Here a side neighbor supports two force chain particles, each through this weak contact. The evolution of Mode 1 versus Mode 2 configurations among the weak MFMC contacts is almost constant throughout loading, especially when compared to the bonded particles in agglomerates A–D. This suggests that there are more reconfigurations in the supporting weak contacts in the fixed contact networks of the agglomerates in (I) prior to fracture. Presumably, this is to compensate for these systems' inability to regulate the confining weak supports to force chains through loss and/or gain of contacts from physical rearrangements of member particles, which happen continually in (II). These grain rearrangements are evident in the average number of contacts per particle fluctuating continually between 3 and 4 [50].

While comparisons between MFMC pathways and force chains are difficult to follow in full 3D space, they are trivial in 2D. Hence we capitalize on the ease of visualization of patterns in System (II) to summarize the trends we observed across *all* the systems studied here, bonded and unbonded. In Fig. 10 (top), we show the percolating MFMC consisting entirely of red and orange edges for one of the representative stages of loading (stage 65 in Fig. 9) for System (II). The contacts in force chains, which were missed by the MFMC, are in blue. Those edges in the MFMC belonging to force chains are in orange; the rest are in red. The red edges consist of strong and weak contacts. The majority in the latter set are in 3-cycles directly supporting a force chain particle in Mode I configuration. With the aid of the zoom-in images of the MFMC as examples [Fig. 10(a)–10(c)], we highlight three recurring patterns in force transmission that are common to all the systems examined. First, in cases where two force chains are right next to each other [e.g., Fig. 10(a)], the MFMC will take the lower cost pathway, often missing one of the force chains (the left chain is favored in this example). Second, the red edges in the MFMC link or join distant as well as proximal force chains (red edges connect orange edges), suggesting the MFMC is indeed correctly identifying paths of optimum force

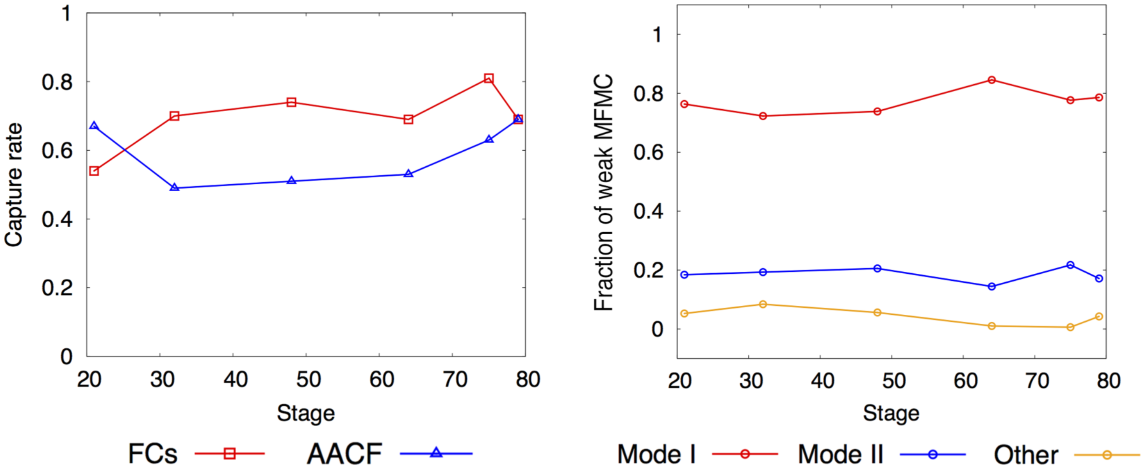

FIG. 9. (Color online) System (II), left: The capture rate of MFMC for the assembly of unbonded photoelastic disks for a model with a uniform capacity and a cost function governed by 3-cycle membership. The average capture rate with respect to force chains is 70%, which is comparable to those obtained in System (I) agglomerates. Right: The fraction of weak MFMC particles in Mode I and Mode II for the assembly of unbonded photoelastic disks.

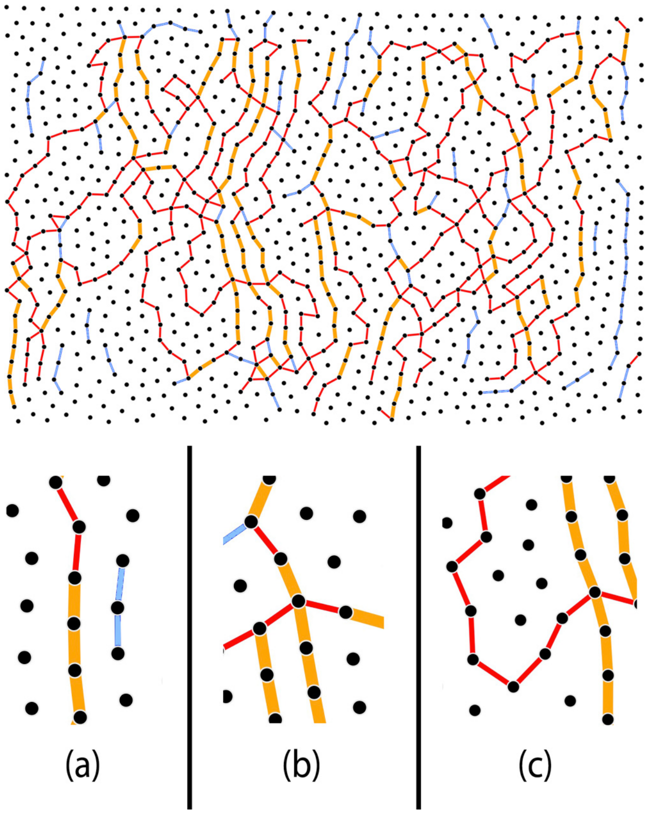

FIG. 10. (Color online) System (II): The percolating MFMC and force chains at a representative stage in the loading history (top). Black dots represent disk centroids. Thin blue edges (thin light grey) are those missed by the MFMC, which belong to force chains. Thick orange (thick dark grey) edges are those that belong to MFMC and are part of force chains. Red edges (thin grey) comprise contacts from both the strong and weak contact network. Zoom-in images of MFMC pathways that are commonly observed across all systems (bottom): (a) When two aligned force chains are located side by side, the MFMC pathway goes through the cheaper route causing one force chain to be missed; (b) independent force chains are often joined together by MFMC pathways; (c) MFMC pathways include direct-quasilinear and as well as tortuous pathways that typically represent intraconnections in force chains and interconnections between force chains, respectively.

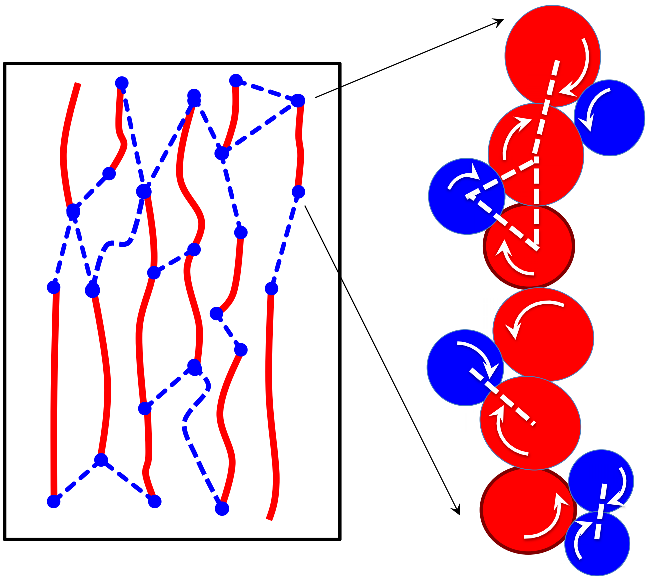

FIG. 11. (Color online) A depiction of the two-tier hierarchical architecture of the percolating MFMC network (left). Local pathways (red) encapsulate *intra*connections between particles in individual force chains and their confining weak contacts in 3-cycles. Global pathways (blue dashed lines with dots at end) encapsulate *inter*connections between distinct force chains. A depiction of some possible intraconnections in a local pathway and frustrated rotations (right). The majority of the weak contacts are in Mode I: A side neighbor supports two force chain particles, one or both of which experiences frustrated rotation (dashed white lines) regardless of the direction of particle rotations in the 3-cycle. A small minority are in Mode II: Two side neighbors support a force chain particle which, depending on the direction of particle rotations, may or may not experience frustrated rotation.

transmission [Fig. 10(b)]. Third, a wide variety of pathways are possible, from the sometimes-tortuous path on the left (red) connecting distant force chains to the direct linear path on the right (orange) which is in fact a force chain [Fig. 10(c)]. These patterns reinforce the fact that the percolating MFMC network is holistic in its description of the major pathways for force transmission. To summarize, the structural elements in force transmission, as defined by the MFMC, embody a two-tier hierarchical architecture, as depicted in Fig. 11. At the local level, it encapsulates *intra*connections between particles in individual force chains and their supporting contacts in conjoined 3-cycles. At the global level, the MFMC encapsulates *inter*connections between force chains, enabling load transfer from one force chain to the next. Geometrically, the direct and quasilinear pathways represent *intra*connections in force chains or *inter*connections between proximal force chains, while tortuous pathways typically connect force chains that are far apart.

VI. CONCLUSION

We developed a family of network flow models of force transmission and tested these on data on microstructural fabric in unbonded as well as bonded granular media. For the bonded systems in 3D, comprising single grain agglomerates, the models depend solely on knowledge of the contacts and the relative bond strengths. For the cohesionless unbonded system in 2D, involving an assembly of unbonded photoelastic disks, the model depends solely on knowledge of the contacts. We solved the maximum flow–minimum cost problem, the solution to which yielded a percolating subnetwork of contacts that transmits the maximum flow (i.e., the highest units of force) at least cost (i.e., the dissipated energy from such transmission). This subnetwork (termed MFMC) represents a network of major force pathways through the global contact network of the material. The best-performing model has these force pathways passing through most of the force chains: Thus the majority of particles in force chains can be predicted through MFMC (i.e., capture rates of 76–82% were observed across all four agglomerates). This model has a capacity function that is based on the bond strength and a cost function that is determined by the local 3-cycle topology. With respect to the composition of this model's MFMC contact network, we find that 76–79% belong to the strong network while the rest belong to the weak network in 3-cycles that directly support force chains. A clear preference is observed for 3-cycle configurations where one side neighbor supports two force chain particles: Here frustrated rotation operates in at least one force chain contact regardless of the direction of rotation of particles in the 3-cycle. For the assembly of unbonded photoelastic disks, comparable, though smaller, capture rates of force chains were found for the same cost function and a uniform capacity. In all the systems studied here, the MFMC embodies a two-tier hierarchical architecture comprising the main structural elements of force transmission. At the local level, it encapsulates *intra*connections between particles in individual columnar force chains and their supporting truss-like 3-cycles; at the global level, the MFMC encapsulates *inter*connections that enable load transfer between force chains. Robustness of trends across these systems suggests the network flow framework may have potential broad utility in the modeling of force transmission in bonded as well as unbonded granular materials. In particular, findings from here and related studies of bottlenecks in force transmission using network flow theory [46–49] pave the way for the prediction of internal forces [59] and the manipulation of granular behavior from the grain scale [60] from data on microstructural fabric. We envisage many opportunities within the framework of network flow to leverage information encoded in high-resolution imaging data for a broad range of granular materials, including cementitious composite materials and loose multicomponent aggregates. We will report on these developments in a future paper.

ACKNOWLEDGMENTS

We thank an anonymous reviewer for helpful suggestions and Reena Kapoor for careful proofreading of the manuscript. This work was supported by the US Army Research Office through Grants No. W911NF1110175 and No. W911NF1110110, the Australian Research Council DP120104759, the Melbourne Energy Institute, the Melbourne Research Grant Support Scheme, The US National Science Foundation through Grant No. CMMI-1362510 to M.C. and K.A., and NSF Grants No. DMR-1206351 and No. DMS-3530656 and NASA Grants No. NNX10AU01G and No. NNX15AD38G to R.P.B..

[1] F. Radjai, D. E. Wolf, M. Jean, and J.-J. Moreau, Phys. Rev. Lett. **80**, 61 (1998).
[2] T. S. Majmudar and R. P. Behringer, Nature **435**, 1079 (2005).
[3] P. Dantu, in *Proceedings of the 4th International Conference on Soil Mechanics and Foundation Engineering* (Butterworths Scientific Publications, London, 1957), Vol. 1, p. 144.
[4] T. Wakabayashi, in *Proceedings of the 7th Japan National Congress for Applied Mechanics, 1957* (University of Tokyo Press, Tokyo, Japan, 1958), pp. 153–158.
[5] A. Drescher and G. de Josselin de Jong, J. Mech. Phys. Solids **20**, 337 (1972).
[6] M. Oda and H. Kazama, Géotechnique **48**, 465 (1998).
[7] A. Tordesillas, Philos. Mag. **87**, 4987 (2007).
[8] A. Tordesillas, J. Zhang, and R. P. Behringer, Geomech. Geoeng. **4**, 3 (2009).
[9] A. Tordesillas, Q. Lin, J. Zhang, R. P. Behringer, and J. Shi, J. Mech. Phys. Solids **59**, 265 (2011).
[10] A. Tordesillas and M. Muthuswamy, J. Mech. Phys. Solids **57**, 706 (2009).
[11] F. Meng, K. Liu, and W. Wang, Tribol. Transact. **58**, 70 (2015).
[12] A. Tordesillas, S. Pucilowski, D. M. Walker, J. F. Peters, and L. E. Walizer, Intl. J. Numer. Anal. Methods Geomech. **38**, 1247 (2014).
[13] D. Bi, J. Zhang, B. Chakraborty, and R. P. Behringer, Nature **480**, 355 (2011).
[14] A. Tordesillas, S. Pucilowski, L. Sibille, F. Nicot, and F. Darve, Philos. Mag. **92**, 4547 (2012).
[15] A. Rechenmacher, S. Abedi, and O. Chupin, Géotechnique **60**, 343 (2010).
[16] K. E. Daniels and N. W. Hayman, J. Geophys. Res.: Solid Earth (1978-2012) **113**, B11411 (2008).
[17] A. Tordesillas, S. Pucilowski, D. M. Walker, J. Peters, and M. Hopkins, Dynam. Cont. Dis. Ser. B **19**, 471 (2012).
[18] A. G. Smart and J. M. Ottino, Soft Matter **4**, 2125 (2008).
[19] P. C. Burnley, Nat. Commun. **4**, 2117 (2013).
[20] N. Guo and J. Zhao, Intl. J. Numer. Methods Eng. **99**, 789 (2014).
[21] N. Brodu, J. A. Dijksman, and R. P. Behringer, Nat. Commun. **6**, 6361 (2015).
[22] M. Kramar, A. Goullet, L. Kondic, and K. Mischaikow, Phys. Rev. E **90**, 052203 (2014).
[23] A. Tordesillas, D. M. Walker, G. Froyland, J. Zhang, and R. P. Behringer, Phys. Rev. E **86**, 011306 (2012).
[24] R. Arévalo, I. Zuriguel, and D. Maza, Phys. Rev. E **81**, 041302 (2010).
[25] L. Kondic, A. Goullet, C. S. O'Hern, M. Kramar, K. Mischaikow, and R. P. Behringer, Europhys. Lett. **97**, 54001 (2012).
[26] D. M. Walker, A. Tordesillas, C. Thornton, R. P. Behringer, J. Zhang, and J. F. Peters, Granul. Matter **13**, 233 (2011).
[27] E. Andò, G. Viggiani, S. A. Hall, and J. Desrues, Géotech. Lett. **3**, 142 (2013).
[28] M. B. Cil and K. A. Alshibli, Géotech. Lett. **2**, 161 (2012).
[29] O. Rozenbaum and S. R. du Roscoat, Phys. Rev. E **89**, 053304 (2014).
[30] J. Zhou, S. Long, Q. Wang, and A. Dinsmore, Science **312**, 1631 (2006).
[31] J. E. Andrade, I. VlahiniĆ, K.-W. Lim, and A. Jerves, Géotech. Lett. **2**, 135 (2012).
[32] M. Saadatfar, A. P. Sheppard, T. J. Senden, and A. J. Kabla, J. Mech. Phys. Solids **60**, 55 (2012).
[33] C. M. Wensrich, E. H. Kisi, V. Luzin, U. Garbe, O. Kirstein, A. L. Smith, and J. F. Zhang, Phys. Rev. E **90**, 042203 (2014).

[34] J. Brujić, S. F. Edwards, D. V. Grinev, I. Hopkinson, D. Brujić, and H. A. Makse, Farad. Discuss. **123**, 207 (2003).

[35] M. M. Mehrabadi, S. Nemat-Nasser, and M. Oda, Intl. J. Numer. Anal. Methods Geomech. **6**, 95 (1982).

[36] G. Meghabghab and A. Kandel, *Search Engines, Link Analysis, and User's Web Behavior: A Unifying Web Mining Approach* (Springer Science and Business Media, Berlin, 2008).

[37] S. Brin and L. Page, Comput. Network. ISDN Syst. **30**, 107 (1998).

[38] A. Tordesillas, D. M. Walker, and Q. Lin, Phys. Rev. E **81**, 011302 (2010).

[39] D. M. Walker, A. Tordesillas, J. Ren, J. A. Dijksman, and R. P. Behringer, Europhys. Lett. **107**, 18005 (2014).

[40] D. M. Walker, A. Tordesillas, J. Zhang, R. P. Behringer, E. Andò, G. Viggiani, A. Druckrey, and K. Alshibli, Intl. J. Solids Struct. **54**, 20 (2015).

[41] D. M. Walker, A. Tordesillas, N. Brodu, J. A. Dijksman, R. P. Behringer, and G. Froyland, Soft Matter **11**, 2157 (2015).

[42] A. Tordesillas, D. M. Walker, E. Andò, and G. Viggiani, Proc. R. Soc. London Ser. A **469**, 20120606 (2013).

[43] R. K. Ahuja, T. L. Magnanti, and J. B. Orlin, *Network Flows: Theory, Algorithms and Applications* (Prentice Hall, Upper Saddle River, NJ, 1993).

[44] M. E. J. Newman, *Networks: An Introduction* (Oxford University Press, Oxford, 2010).

[45] W. J. Cook, W. H. Cunningham, W. R. Pulleyblank, and A. Schrijver, *Combinatorial Optimization* (Wiley-Interscience, New York, 1998).

[46] A. Tordesillas, A. Cramer, and D. M. Walker, Powders and Grains 2013, AIP Conf. Proc. **1542**, 507 (2013).

[47] Q. Lin and A. Tordesillas, Powders and Grains 2013, AIP Conf. Proc. **1542**, 547 (2013).

[48] Q. Lin and A. Tordesillas, J. Ind. Manag. Optim. **10**, 337 (2014).

[49] A. Tordesillas, S. Pucilowski, S. Tobin, M. R. Kuhn, E. Ando, G. Viggiani, A. Druckrey, and K. Alshibli, Europhys. Lett. (to be published).

[50] J. Zhang, T. S. Majmudar, A. Tordesillas, and R. P. Behringer, Granul. Matter **12**, 159 (2010).

[51] D. E. Wolf, F. Radjai, and S. Dippel, Philos. Mag. **77**, 1413 (1998).

[52] D. M. Walker, A. Tordesillas, and G. Froyland, Phys. Rev. E **89**, 032205 (2014).

[53] D. O. Potyondy and P. A. Cundall, Intl. J. Rock Mech. Min. Sci. **41**, 1329 (2004).

[54] E. W. Weisstein, Lambert azimuthal equal-area projection, Wolfram Mathworld, http://mathworld.wolfram.com/LambertAzimuthalEqual-AreaProjection.html.

[55] L. R. Ford and D. R. Fulkerson, Can. J. Math. **8**, 399 (1956).

[56] A. A. Hagberg, D. A. Schult, and P. J. Swart, in *Proceedings of the 7th Python in Science Conference (SciPy2008)*, edited by G. Varoquaux, T. Vaught, and J. Millman (Pasadena, CA, USA, 2008), pp. 11–15.

[57] M. Muthuswamy and A. Tordesillas, J. Stat. Mech. Theor. Exp. (2006) P09003.

[58] J. F. Peters, M. Muthuswamy, J. Wibowo, and A. Tordesillas, Phys. Rev. E **72**, 041307 (2005).

[59] S. T. Tobin, A. Tordesillas, A. Druckrey, M. Cil, K. Alshibli, N. Brodu, J. A. Dijksman, and R. P. Behringer (unpublished) (2015).

[60] D. M. Walker, A. Tordesillas, T. Nakamura, and T. Tanizawa, Phys. Rev. E **87**, 032203 (2013).